Multilevel analysis of spatiotemporal association features for differentiation of tumor enhancement patterns in breast DCE-MRI

Sang Ho Lee
Interdisciplinary Program in Radiation Applied Life Science, Seoul National University College of Medicine, and Institute of Radiation Medicine, Seoul National University Medical Research Center, Seoul 110-744, Korea

Jong Hyo Kim[a)]
Department of Radiology, Seoul National University College of Medicine, Seoul 110-744, Korea

Nariya Cho and Jeong Seon Park[b)]
Department of Radiology, Seoul National University Hospital, Seoul 110-744, Korea

Zepa Yang
Department of Biomedical Sciences, Seoul National University College of Medicine, Seoul 110-744, Korea

Yun Sub Jung
Interdisciplinary Program in Radiation Applied Life Science, Seoul National University College of Medicine, Seoul 110-744, Korea

Woo Kyung Moon
Department of Radiology, Seoul National University College of Medicine, Seoul, 110-744, Korea

Purpose: Analyzing spatiotemporal enhancement patterns is an important task for the differential diagnosis of breast tumors in dynamic contrast-enhanced MRI (DCE-MRI), and yet remains challenging because of complexities in analyzing the time-series of three-dimensional image data. The authors propose a novel approach to breast MRI computer-aided diagnosis (CAD) using a multilevel analysis of spatiotemporal association features for tumor enhancement patterns in DCE-MRI.
Methods: A database of 171 cases consisting of 111 malignant and 60 benign tumors was used. Time-series contrast-enhanced MR images were obtained from two different types of MR scanners and protocols. The images were first registered for motion compensation, and then tumor regions were segmented using a fuzzy c-means clustering-based method. Spatiotemporal associations of tumor enhancement patterns were analyzed at three levels: Mapping of pixelwise kinetic features within a tumor, extraction of spatial association features from kinetic feature maps, and extraction of kinetic association features at the spatial feature level. A total of 84 initial features were extracted. Predictable values of these features were evaluated with an area under the ROC curve, and were compared between the spatiotemporal association features and a subset of simple form features which do not reflect spatiotemporal association. Several optimized feature sets were identified among the spatiotemporal association feature group or among the simple feature group based on a feature ranking criterion using a support vector machine based recursive feature elimination algorithm. A least-squares support vector machine (LS-SVM) classifier was used for tumor differentiation and the performances were evaluated using a leave-one-out testing.
Results: Predictable values of the extracted single features ranged in 0.52–0.75. By applying multilevel analysis strategy, the spatiotemporal association features became more informative in predicting tumor malignancy, which was shown by a statistical testing in ten spatiotemporal association features. By using a LS-SVM classifier with the optimized second and third level feature set, the CAD scheme showed A_z of 0.88 in classification of malignant and benign tumors. When this performance was compared to the same LS-SVM classifier with simple form features which do not reflect spatiotemporal association, there was a statistically significant difference (0.88 vs 0.79, $p < 0.05$), suggesting that the multilevel analysis strategy yields a significant performance improvement.
Conclusions: The results suggest that the multilevel analysis strategy characterizes the complex tumor enhancement patterns effectively with the spatiotemporal association features, which in turn leads to an improved tumor differentiation. The proposed CAD scheme has a potential for improving diagnostic performance in breast DCE-MRI. © *2010 American Association of Physicists in Medicine*. [DOI: 10.1118/1.3446799]

I. INTRODUCTION

Dynamic contrast-enhanced (DCE) breast MRI is being applied for detection, diagnosis, and staging of breast cancer. As breast DCE-MRI is recently recommended as a screening option of breast cancer for women at high risk,[1–6] differentiation of malignant and benign tumors is becoming a more important function in breast DCE-MRI.

The breast DCE-MRI produces a high spatial resolution and time course imaging data on contrast enhancements of a tumor and its surrounding tissue. The abundance of information it provides is potentially capable of differentiation between malignant and benign tumors.[7]

In principle, the contrast enhancement kinetics and morphological features in breast DCE-MRI provide valuable information for diagnosing suspected malignancy of breast tumors.[8] Previous studies have reported the efficacy of contrast enhancement kinetics in evaluating tumor vascularization, which has been correlated with biological and clinical aggressiveness.[9,10] The differences in tumor vascularity present varying degrees of contrast enhancement patterns in DCE-MRI according to their malignancy; malignant lesions typically exhibit early strong enhancement with rapid washout, whereas benign lesions usually show a slow increase followed by persistent enhancement.[9] Morphological criteria have also been verified as valuable diagnostic tools in differential diagnosis of breast tumors.[11,12] Spiculate margin, internal heterogeneous or rim enhancement, and irregular shape are important predictors of malignancy, whereas smooth margin, internal homogeneous enhancement, and regular shape are related to benignancy in general.[8]

In conventional practice, kinetic and morphological features are evaluated in subjective ways. The majority of kinetic analysis for breast tumors has been carried out on manual placement of a region of interest (ROI) within a tumor.[9,13,14] Various morphological features are also evaluated in subjective ways based on observer experience. Although the Breast Imaging Reporting and Data System lexicon provides useful criteria on visual assessment of various tumor morphologies,[15] priority and weights on different morphological features are not standardized. In addition, visual assessment of time-series image data containing complex spatiotemporal features by radiologists is a time consuming task and imposes another impediment.

In order to overcome such limits, considerable efforts have been put on the development of computer-aided diagnosis (CAD) algorithms. For objective classification of kinetic features from the ROI, Lucht *et al.*[16] applied artificial neural network and Levman *et al.*[17] introduced support vector machine (SVM). For quantitative evaluation of morphological features, Gilhuijs *et al.*[18] employed radial gradient histogram and other shape measures. Studies have also been conducted to include both kinetic and morphological features

in CAD schemes. Chen *et al.*[19] analyzed dynamics of enhancement variance within segmented tumors and Meinel *et al.*[20] used backpropagation neural network to classify a combined set of shape and kinetic features from the segmented tumor region. Recently, Zheng *et al.*[21,22] applied discrete Fourier transformation (DFT) to kinetic curves and extracted Hu's moment invariants from the DFT coefficients of selected two-dimensional images.

A major challenge in the diagnosis of breast DCE-MRI is to analyze the complexity on the spatiotemporal association of tumor enhancement patterns. In fact, the morphological pattern of a tumor in DCE-MRI dynamically changes due to diverse time courses of signal enhancement at each pixel. Likewise, the kinetic patterns of enhancement are different on various parts within a tumor. In most previous studies, however, the associations between spatial and temporal features were rarely investigated, and these features were treated separately; the morphological features were extracted at a specific time point assuming they are fixed; when extracting the kinetic features, their spatial dependency was also mostly neglected.

In this study, we postulate that analyzing spatiotemporal associations of tumor enhancement patterns would gain additional information otherwise not attainable, and thus may allow an improved performance for tumor differentiation. Based on this postulation, we propose a novel approach to breast MRI CAD using multilevel analysis of spatiotemporal association features for tumor enhancement patterns in DCE-MR images.

II. MATERIALS AND METHODS

II.A. Patients

A total of 171 female patients [mean age, 46.7 yr ± 8 (SD); range, 25–74 yr] were included in this retrospective study, from which one primary lesion per patient was used for analysis. All patients were seen in our radiology department for mammographic and/or sonographic abnormalities and underwent breast DCE-MRI at our institution between January 2004 and December 2009.

Our database consisted of two data sets: Data set 1 of 75 patients [mean age, 45.6 yr ± 8 (SD); range, 25–61 yr], obtained with a MR scanner 1 (Magnetom Sonata; Siemens, Erlangen, Germany) during January 2004 and December 2006; and data set 2 of 96 patients [mean age, 47.5 yr ± 8 (SD); range, 32–74 yr), obtained with a MR scanner 2 (Signa; GE Medical Systems, Milwaukee, WI) during January 2007 to December 2009. As a total, our database contained 111 malignant and 60 benign lesions. All malignant lesions and 52 benign lesions were proved by histological examination using surgically excised specimens and eight benign lesions were confirmed by core biopsies or follow-up exami-

TABLE I. Distribution of the malignant and benign lesions according to the histopathologic types in data sets 1 and 2.

| Data set 1 | | | | Data set 2 | | | | Pooled data set | | | |
| MR scanner 1 | | | | MR scanner 2 | | | | MR scanner 1/MR scanner 2 | | | |
Malignant	No. of lesions	Benign	No. of lesions	Malignant	No. of lesions	Benign	No. of lesions	Malignant	No. of lesions	Benign	No. of lesions
Invasive ductal carcinoma	36	Fibroadenoma	6	Invasive ductal carcinoma	20	Fibroadenoma	13	Invasive ductal carcinoma	56	Fibroadenoma	19
Invasive lobula carcinoma	9	Fibrocystic change	2	Invasive lobula carcinoma	15	Fibrocystic change	8	Invasive lobula carcinoma	24	Fibrocystic change	10
Ductal carcinoma *in situ*	6	Papilloma	3	Ductal carcinoma *in situ*	18	Papilloma	6	Ductal carcinoma *in situ*	24	Papilloma	9
		Phyllodes tumor	3	Metaplastic carcinoma	5			Metaplastic carcinoma	5	Phyllodes tumor	3
		Hamartoma	1	Mucinous carcinoma	2	Hamartoma	1	Mucinous carcinoma	2	Hamartoma	2
		Atypical hyperplasia	1			Atypical hyperplasia	1			Atypical hyperplasia	2
						Other benign mass	7			Other benign mass	7
		Follow-up	8							Follow-up	8
Subtotal	51	Subtotal	24	Subtotal	60	Subtotal	36	Total	111	Total	60

nations for at least 1 yr. The follow-up consisted of mammography, sonography, and MRI at intervals of six months for the first 1 yr.

Data set 1 included 51 malignant and 24 benign lesions. The 51 malignant lesions were 36 invasive ductal carcinomas (IDCs), nine invasive lobular carcinomas (ILCs), and six ductal carcinomas *in situ* (DCISs). Among the 24 benign lesions, 16 lesions were histologically confirmed: Six fibroadenomas, two fibrocystic changes, three papillomas, three phyllodes tumors, one hamartoma, and one atypical hyperplasia. Data set 2 included 60 malignant and 36 benign lesions. The 60 malignant lesions were: 20 IDCs, 15 ILCs, 18 DCISs, five metaplastic carcinomas, and two mucinous carcinomas. The 36 benign lesions contained 13 fibroadenomas, eight fibrocystic changes, six papillomas, one hamartoma, one atypical hyperplasia, and seven other benign masses. The distribution of the histological findings in our database is summarized in Table I.

II.B. MR imaging

MR imaging was performed with the patients in a prone position using a dedicated phase-array breast coil. MR scanner 1 was used to scan 75 patients in data set 1. The contrast agent gadopentetate dimeglumine (Magnevist; Schering, Berlin, Germany) was administered intravenously by power injection with a dose of 0.1 mmol/kg bodyweight at a flow rate of 2 ml/s for 5 s. T_1-weighted three-dimensional fast low angle shot (3D FLASH) dynamic sequences were performed with one pre-enhanced and four postenhanced series in a

unilateral sagittal volume scan. The imaging parameters were: Repetition time/echo time, 4.9/1.83 ms; flip angle, 12°; field of view, 170×170 mm^2; matrix size, 448×448; in-plane resolution, 0.38×0.38 mm^2; slice thickness, 1–1.5 mm without a gap; and number of sagittal slices, 96–112. The acquisition time of each volume sequence was 1.4 min and the dynamic series were consecutively scanned without delay after contrast injection. Thus, the first postcontrast time point occurred 1.4 min (in terms of full k-space acquisition time) after the injection, followed by 2.8, 4.2, and 5.6 min postcontrast time points (third to fifth scans).

MR scanner 2 was used for 96 patients in data set 2. The contrast agent gadobutrol (Gadovist; Schering, Berlin, Germany) was administered intravenously by power injection with a dose of 0.1 mmol/kg bodyweight at a flow rate of 2 ml/s for 5 s. T_1-weighted 3D spoiled gradient-echo (SPGR) sequences were performed with one precontrast and five postcontrast series in a bilateral sagittal volume scan. The imaging parameters were: Repetition time/echo time, 6.5/2.5 ms; flip angle, 10°; field of view, 180×180 to 200×200 mm^2; matrix size, 512×512; in-plane resolution, 0.35×0.35 to 0.39×0.39 mm^2; slice thickness, 1.4–1.5 mm without a gap; and number of sagittal slices, 144–208. The acquisition time of each volume sequence was 1 min and the dynamic series were scanned without delay, and then with 1.5, 4.5, 6, and 8 min delay after contrast injection, respectively. Thus, the first postcontrast time point occurred 1 min (in terms of full k-space acquisition time) after the injection, followed by 2.5, 5.5, 7, and 9 min postcontrast time points

TABLE II. MR imaging protocols used for image acquisition in the study.

Imaging parameter	MR scanner 1	MR scanner 2
Contrast agent	Gadopentetate dimeglumine	Gadobutrol
Dose (mmol/kg)	0.1	0.1
Injection rate (ml/s)	2	2
Injection duration (s)	5	5
B_0 field strength (T)	1.5	1.5
Pulse sequence	T_1-weighted 3D FLASH	T_1-weighted 3D SPGR
Scan coverage	Unilateral	Bilateral
Plane	Sagittal	Sagittal
TR/TE (ms)	4.9/1.83	6.5/2.5
Flip angle (deg)	12	10
Field of view (mm^2)	170×170	180×180 to 200×200
Matrix size (pixel)	448×448	512×512
In-plane resolution (mm^2)	0.38×0.38	0.35×0.35 to 0.39×0.39
Slice thickness (mm)	1–1.5	1.4–1.5
No. of slices/gap	96 to 112/No	144 to 208/No
Volume scan time (min)	1.4	1
Dynamic acquisition time (min)	1.4, 2.8, 4.2, 5.6	1, 2.5, 5.5, 7, 9
No. of postcontrast series	4	5

(third to sixth scans). Details of the two different MR imaging protocols used in the analysis are summarized in Table II.

II.C. Image registration

In order to reduce possible artifacts or blurring due to the patient motion, we aligned all postcontrast series to the precontrast one (first series) of the dynamic sequences using a 3D rigid registration technique based on the maximization of mutual information.[23] The registered MR images were visually inspected and evaluated by two experienced and highly trained radiologists in consensus and confirmed to be helpful for motion compensation.

II.D. Tumor segmentation

For breast tumor segmentation on DCE-MR images, a box-shaped 3D volume of interest (VOI) was selected to contain the lesion by a human operator for each case. The size of a rectangle bounding the lesion in each slice level was determined by the largest extent of the lesion shown in a representative middle slice. And then, a fuzzy c-means (FCM) clustering algorithm was applied to segment tumor out of background tissue.[24,25] While FCM clustering was usually performed using vector data to represent time-series data in previous studies, we employed a scalar value in this study that extract more compact information from all time-series data in order to be better applicable to our two data sets having different temporal acquisition protocols.

A scalar signal, denoted as variance of enhancement slope (VES), was used to represent the pharmacokinetic activity at each pixel.[26] The VES is given as the following expression:

$$\text{VES} = \text{Var}\left(\frac{I_t - I_0}{t}\right), \quad 0 < t \le M, \tag{1}$$

where t denotes the time elapsed (min) from contrast injection and M is the elapsed time of the last temporal phase,

which was 5.6 for data set 1 and 9 for data set 2 in this study. I_0 and I_t indicate the precontrast and postcontrast signal intensity taken at time t, respectively. $\text{Var}(\cdot)$ indicates the variance of enhancement slope data over all available t. A volumetric image was generated to map the VES value at each pixel. The selected examples of VES maps generated using Eq. (1) are shown in Fig. 1, where enhanced tumor-to-
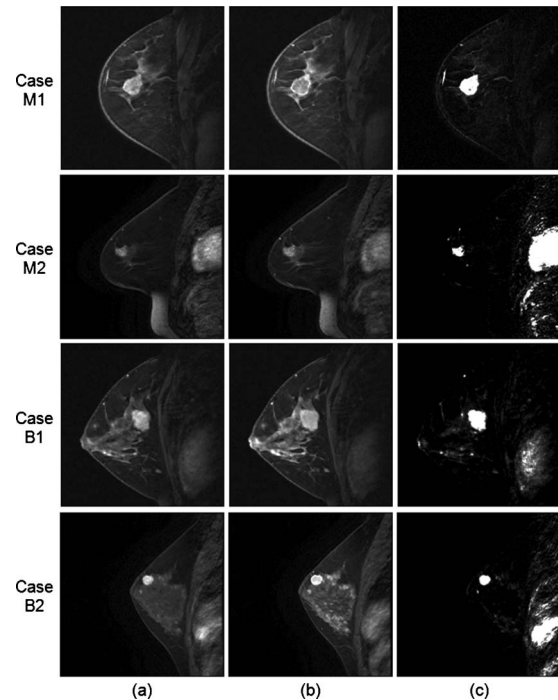

FIG. 1. Example of the proposed VES map images: (a) Initial postcontrast, (b) fourth postcontrast, and (c) VES map images. Upper two rows are malignant cases: M1 (IDC) and M2 (DCIS), while lower two rows are benign cases: B1 (phyllodes tumor) and B2 (fibroadenoma). Note that enhanced tumor contrast appears in the VES map images.

parenchyma contrast is demonstrated in both malignant and benign cases.

The FCM clustering algorithm is a fuzzy equivalent to the "hard" k-means clustering, where the assignment of fuzzy membership values can serve as a confidence measure in tumor segmentation. Let $X = \{x_i, i = 1, 2, \cdots, N | x_i \in \mathfrak{R}\}$ denote the input data set compromising N pixels to be partitioned into c clusters. In this study, the data point x_i was the scalar value of VES at pixel i within the 3D VOI. The FCM clustering was applied to partition the VOI pixels into two categories ($c = 2$): Tumor and background parenchyma. Fuzzy partitioning for breast tumor segmentation was carried out through an iterative optimization to minimize the within-group error function J defined as

$$J = \sum_{k=1}^{2} \sum_{i=1}^{N} u_{ki}^2 \|x_i - v_k\|^2, \tag{2}$$

with the following constraints:

$$\sum_{k=1}^{2} u_{ki} = 1, \quad \forall i; 0 \le u_{ki} \le 1, \quad \forall k,$$

$$i; \sum_{i=1}^{N} u_{ki} > 0, \quad \forall k, \tag{3}$$

where N is the number of pixels in the 3D VOI, u_{kj} is the membership probability that x_i belongs to cluster k, v_k is the kth cluster center obtained from weighted averaging of x_i, and $\|\cdot\|$ denotes the Euclidean distance expressing the similarity between any measured data and the center, respectively. The within-group error function J is minimized when high membership values are assigned to the pixels close to the centroids of clusters, and low membership values to the pixels far from the centroids. The membership probability depends on the distance between the pixel and each individual cluster center in the feature domain. In our implementation, starting with random assignment of the membership probability u_{ki}, the center vector v_k was initially guessed and then u_{ki} and v_k were iteratively updated by the following equations:

$$u_{ki} = \frac{1}{\sum\limits_{l=1}^{2} \left(\dfrac{\|x_i - v_k\|}{\|x_i - v_l\|} \right)^2}, \quad k = 1, 2; i = 1, 2, \cdots, N, \tag{4}$$

$$v_k = \frac{\sum\limits_{i=1}^{N} u_{ki}^2 x_i}{\sum\limits_{i=1}^{N} u_{ki}^2}, \quad k = 1, 2. \tag{5}$$

The iterative optimization was stopped when

$$\max_{ki} \|u_{ki}^{(r+1)} - u_{ki}^{(r)}\| < \varepsilon, \tag{6}$$

where ε ($\varepsilon = 10^{-5}$ in this study) is a termination criterion and r denotes the iteration steps. The v_k was used to determine which k represented the lesion class. If $l = \arg \max_k(v_k)$, u_{li}
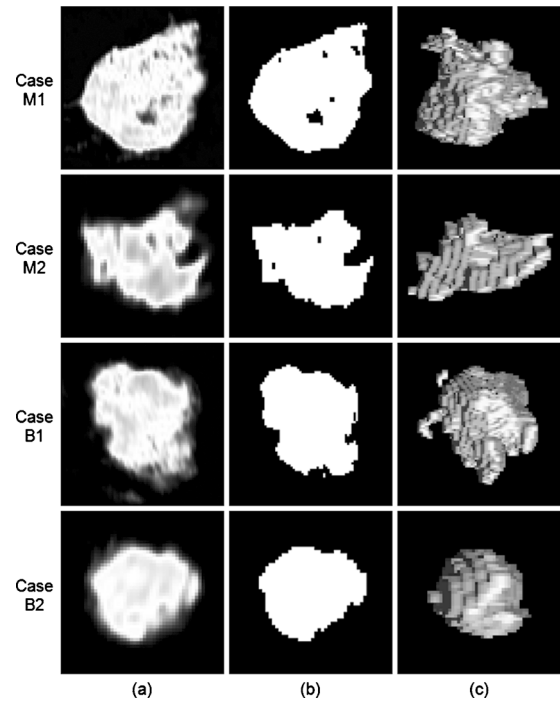
FIG. 2. Lesion segmentation using FCM: (a) Lesion membership map from FCM, (b) binarized results, and (c) surface rendered images after lesion segmentation. The lesion samples are corresponding to the rows in the same order in Fig. 1.

and v_l were the membership probability and cluster center of the lesion class, respectively.

The lesion membership map resulting from the FCM clustered VOI was binarized with an experimentally determined threshold TH = 0.6, which was consistently applied to all tumors in our database. If u_{li} at pixel i was larger than TH, the pixel was assigned to the tumor. Within the 3D VOI, the largest 3D connected component based on 26 pixel connectivity was selected and the other pixels were grouped into the background. Some examples of the lesion membership map,
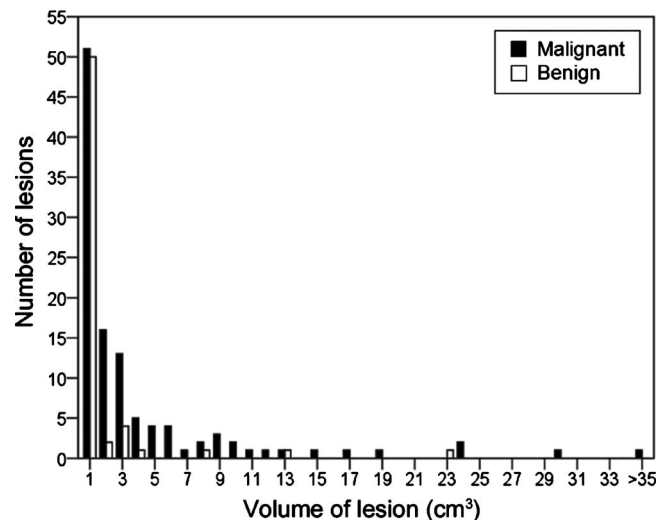

FIG. 3. Distribution of lesion volumes for all malignant and benign lesions in the breast MR imaging database.
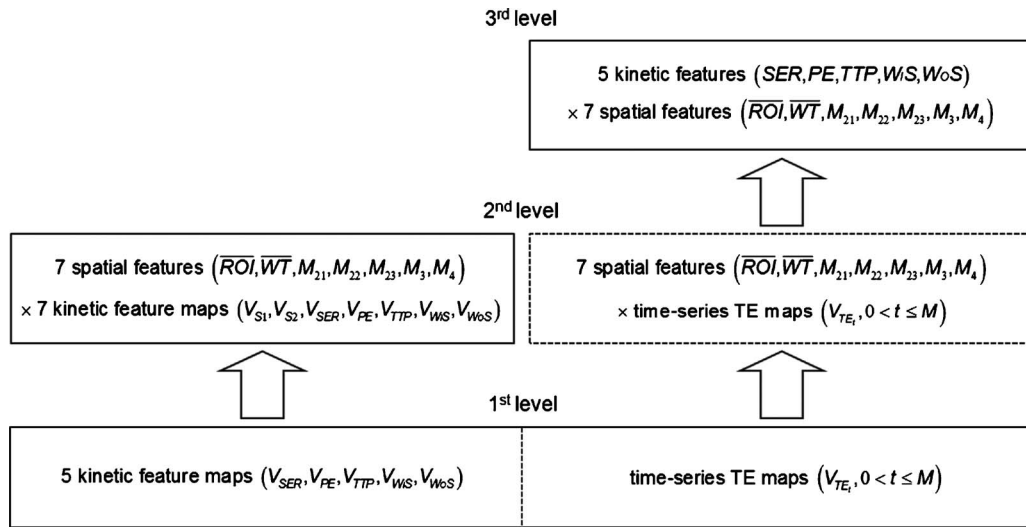
FIG. 4. Illustration of the spatiotemporal feature extraction process at three levels. Five kinetic feature maps and time-series TE maps are generated on a pixelwise basis at the first level. The seven kinetic feature maps (V_{S1}, V_{S2}, V_{SER}, V_{PE}, V_{TTP}, $V_{W_I S}$, and $V_{W_O S}$) are selected for use at the second level and the time-series TE maps (V_{TE_t}, $0 < t \leq M$) are used for the third level analysis. Note that V_{S1} and V_{S2} are the TE maps selected from V_{TE_t} ($0 < t \leq M$) in the 3TP method. Seven spatial features ($\overline{ROI}$, $\overline{WT}$, M_{21}, M_{22}, M_{23}, M_3, and M_4) are extracted from the seven kinetic feature maps at the second level to evaluate spatial association of temporal signals, and then five kinetic features (SER, PE, TTP, $W_I S$, and $W_O S$) are extracted from the seven spatial features at the third level to evaluate the kinetic association of each spatial feature.

binarized results, and corresponding 3D mass contour are shown in Fig. 2. The resulting segmented lesions had a mean size of 3.014 cm^3 with standard deviation of 7.942 cm^3. Figure 3 shows the distribution of tumor volumes for all of the lesions included in this study.

II.E. Multilevel extraction of spatiotemporal association features

We regarded it as essential to extract informative features related to spatiotemporal association of intratumoral enhancement patterns for effective differentiation of malignant and benign tumors in DCE-MRI. More specifically, we modeled the tumor enhancement as a signal distribution in 4D spatiotemporal space, wherein the characteristic information of a tumor is scattered throughout. Therefore, it is required to develop a sophisticated model to efficiently capture various aspects of tumor information scattered in the spatiotemporal enhancement patterns. In this study, we used a three-level approach to analyze various aspects of spatiotemporal association of tumor enhancement patterns: Pixelwise kinetic feature mapping, extraction of spatial association features from pixelwise kinetic feature maps, and extraction of kinetic association features at the spatial feature level. An illustration of the three-level spatiotemporal extraction procedure is shown in Fig. 4.

II.E.1. First level: Pixelwise kinetic feature mapping

At the first level, various kinetic features were calculated for each pixel within a tumor: Temporal enhancement at each temporal phase (TE$_t$), peak enhancement (PE), time-to-peak (TTP), wash-in slope (W$_I$S), wash-out slope (W$_O$S), and

three additional features ($S1$, $S2$, and SER) according to three-time-points (3TP) method.[19,27–29] The TE at each temporal phase is defined by

$$\mathrm{TE}_t = \frac{I_t - I_0}{I_0}, \quad 0 < t \leq M, \tag{7}$$

where t and M are the same as Eq. (1). The PE is the maximum value among all TEs (PE$= \max_{0<t\leq M} \mathrm{TE}_t$), and TTP is the time at which the PE occurs. The W$_I$S and W$_O$S are, respectively, defined as

$$\mathrm{W_I S} = \frac{\mathrm{PE}}{\mathrm{TTP}}, \tag{8}$$

$$\mathrm{W_O S} = \begin{cases} \dfrac{\mathrm{PE} - \mathrm{TE}_M}{M - \mathrm{TTP}} & (\mathrm{TTP} \neq M) \\ 0 & (\mathrm{TTP} = M) \end{cases}, \tag{9}$$

where TE$_M$ denotes the TE at the last postcontrast time. The $S1$, $S2$, and SER are the parameters of a TE curve at each pixel defined in the 3TP method. The selection of the 3TP is known to be accomplished by model-based calculations that provide optimal discrimination between malignant and benign tumors.[27,30] In our implementation, $S1$ was chosen as the TE taken between 1 and 2 min (1.4 min for data set 1; 1 min for data set 2) and $S2$ as the TE taken between 5 and 7 min (5.6 min for data set 1; 7 min for data set 2).[31,32] The SER was the signal enhancement ratio defined as $S1/S2$.[27–29] Then, we created volumetric images to map these basic kinetic features at each pixel on a tumor, which were used for subsequent feature extraction steps. V_{TE_t} denotes the volumetric image for the TE map at time t, V_{S1} for the $S1$ map,
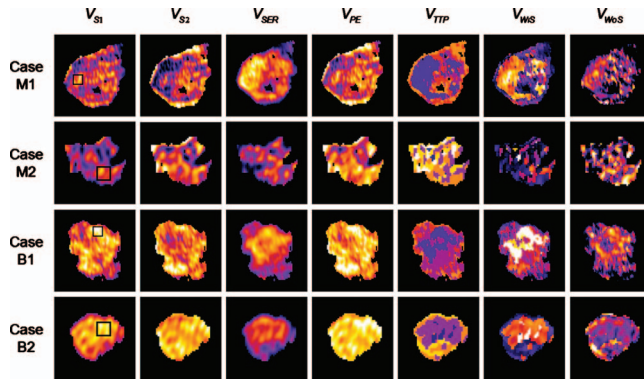
FIG. 5. Examples of pixelwise kinetic feature map images. V_{S1} is an image for $S1$ map, V_{S2} for $S2$ map, V_{SER} for SER map, V_{PE} for PE map, V_{TTP} for TTP map, V_{W_IS} for W_IS map, and V_{W_OS} for W_OS map. A typical slice was selected to visualize the spatial distribution of pseudocolored kinetic features within tumors. Rim enhancements are seen in case M1 at V_{S1}, V_{S2}, V_{PE}, and V_{TTP}, along with a later wash-out seen at V_{SER} and V_{W_OS}, which are typical enhancement patterns of the malignant tumor. Case M2 shows heterogeneous area enhancements at V_{S1} and V_{S2}, which is another important pattern of the malignant tumor. Case B1 has early central enhancements seen at V_{S1} and V_{W_IS} along with delayed peripheral filling seen at V_{S2}. Case B2 shows the relatively homogeneous enhancement pattern, which is a typical enhancement pattern of a benign tumor. Small boxes (9×9 pixel square masks) in V_{S1} are the most enhancing ROIs. Note that the kinetic feature maps represent the scaled size for visual convenience. The tumor samples are corresponding to the rows in the same order of those in Fig. 2.

V_{S2} for the S2 map, V_{SER} for the SER map, V_{PE} for the PE map, V_{TTP} for the TTP map, V_{W_IS} for the W_IS map, and V_{W_OS} for the W_OS map. Figure 5 shows example images of pixelwise kinetic feature maps for selected cases.

II.E.2. Second level: Extraction of spatial association features

At the second level, seven spatial features were calculated for the volumetric images of the pixelwise kinetic features produced at the first level: Mean values of the most enhancing ROI and whole tumor (WT) and five 3D moment invariants. As our database consisted of two data sets, which were acquired with two different MRI machines that produced different number of postcontrast images at different time points, we determined to include only those features which represent common meaning from the two subdata sets. The selected features were seven spatial features calculated from seven kinetic feature map images such as V_{S1}, V_{S2}, V_{SER}, V_{PE}, V_{TTP}, V_{W_IS}, and V_{W_OS}.

II.E.2.a. Mean of ROI. A ROI of a 9×9 pixel square mask (3.15×3.15 to 3.51×3.51 mm^2) was automatically selected on a location having the highest mean value in the V_{S1} image for each tumor and was used to obtain mean values within the most enhancing ROI (denoted as $\overline{\text{ROI}}$).[33,34] The same ROI location was used to obtain the $\overline{\text{ROI}}$ on the pixelwise kinetic feature map images for each tumor. The seven $\overline{\text{ROI}}$s were $\overline{\text{ROI}}(V_{S1})$, $\overline{\text{ROI}}(V_{S2})$, $\overline{\text{ROI}}(V_{SER})$, $\overline{\text{ROI}}(V_{PE})$, $\overline{\text{ROI}}(V_{TTP})$, $\overline{\text{ROI}}(V_{W_IS})$, and $\overline{\text{ROI}}(V_{W_OS})$.

II.E.2.b. Mean of whole tumor. Mean values of a whole tumor ($\overline{\text{WT}}$) were obtained by taking the volumetric average of pixelwise kinetic feature values within the tumor.[35] The
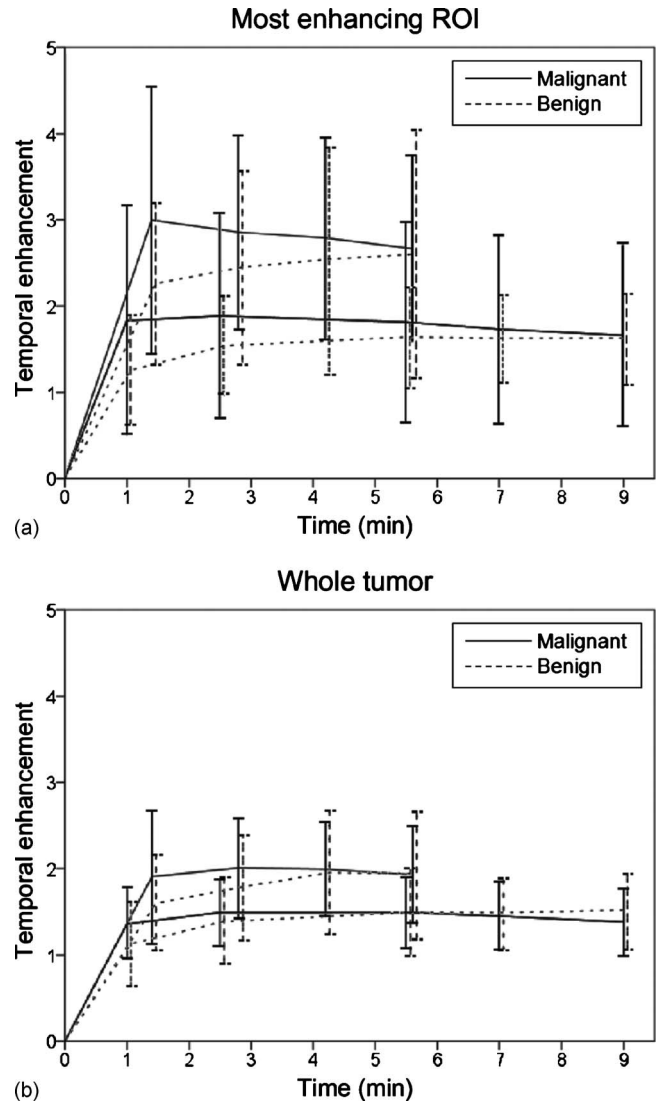

FIG. 6. Distribution of time enhancement curves for (a) mean ROI and (b) mean WT values. The four postenhanced curves are resulted from the data set 1, while the five postenhanced curves form the data set 2. Solid lines are for malignant tumors and dotted lines for benign tumors. Error bars indicate the ± 1 standard deviation of the TE values in each time point.

seven $\overline{\text{WT}}$s were $\overline{\text{WT}}(V_{S1})$, $\overline{\text{WT}}(V_{S2})$, $\overline{\text{WT}}(V_{SER})$, $\overline{\text{WT}}(V_{PE})$, $\overline{\text{WT}}(V_{TTP})$, $\overline{\text{WT}}(V_{W_IS})$, and $\overline{\text{WT}}(V_{W_OS})$. Distributions of time enhancement curves for $\overline{\text{ROI}}$s and $\overline{\text{WT}}$s are compared between malignant and benign tumors in Fig. 6.

II.E.2.c. 3D moment invariants. We adopted a 3D moment invariant (3D MI) method for describing the spatial distribution patterns of pixelwise kinetic feature maps within a tumor. The intensity value of a pixel in a volumetric feature map image is represented as a density function $\rho(x,y,z)$ of Cartesian coordinate system. Then, the 3D moments of a density function $\rho(x,y,z)$ are defined as

$$m_{pqr} = \int_{-\infty}^{\infty} \int_{-\infty}^{\infty} \int_{-\infty}^{\infty} x^p y^q z^r \rho(x,y,z) dx dy dz, \qquad (10)$$

where $n = p + q + r$ is the order of the moment. In addition, invariant transformations were applied to the 3D moments in

order to capture unique spatial features independent to shift, rotation, or scale caused by variations in patient postures or particular coordinate system used in imaging system. The translational invariance was obtained by using central moments defined as

$$\mu_{pqr} = \int_{-\infty}^{\infty} \int_{-\infty}^{\infty} \int_{-\infty}^{\infty} (x - \bar{x})^p (y - \bar{y})^q (z - \bar{z})^r \rho(x,y,z) dx dy dz,$$

(11)

where $\bar{x}$, $\bar{y}$, and $\bar{z}$ are the centroid coordinates of the density function $\rho(x,y,z)$, calculated as

$$\bar{x} = \frac{m_{100}}{m_{000}}, \quad \bar{y} = \frac{m_{010}}{m_{000}}, \quad \bar{z} = \frac{m_{001}}{m_{000}}.$$

(12)

For scale invariance, the central moments were additionally normalized as follows:

$$\eta_{pqr} = \frac{\mu_{pqr}}{\mu_{000}^{[(p+q+r)/3]+1}}.$$

(13)

In order to obtain rotational invariance, the normalized central moments were transformed into linear combinations of moments of the same order. A total of five 3D MIs were used in this study, three of which were based on the second order moments derived by Sadjadi and Hall,[36] and the remaining higher order MIs were derived based on moment tensor contraction according to Ng *et al.*[37] With the normalized 3D central moments, the second order 3D MIs can be written as

$$M_{21} = \eta_{200} + \eta_{020} + \eta_{002},$$

(14)

$$M_{22} = \eta_{200}\eta_{020} + \eta_{200}\eta_{002} + \eta_{020}\eta_{002} - \eta_{101}^2 - \eta_{110}^2 - \eta_{011}^2,$$

(15)

$$M_{23} = \eta_{200}\eta_{020}\eta_{002} - \eta_{002}\eta_{110}^2 + 2\eta_{110}\eta_{101}\eta_{011} - \eta_{020}\eta_{101}^2 - \eta_{200}\eta_{011}^2.$$

(16)

The derived higher order 3D MIs are as follows:

$$M_3 = \eta_{300}^2 + \eta_{030}^2 + \eta_{003}^2 + 3\eta_{210}^2 + 3\eta_{201}^2 + 3\eta_{120}^2 + 6\eta_{111}^2 + 3\eta_{102}^2 + 3\eta_{021}^2 + 3\eta_{012}^2,$$

(17)

$$M_4 = \eta_{400}^2 + \eta_{040}^2 + \eta_{004}^2 + 4\eta_{310}^2 + 4\eta_{301}^2 + 6\eta_{220}^2 + 12\eta_{211}^2 + 6\eta_{202}^2 + 4\eta_{130}^2 + 12\eta_{121}^2 + 12\eta_{112}^2 + 4\eta_{103}^2 + 4\eta_{031}^2 + 6\eta_{022}^2 + 4\eta_{013}^2.$$

(18)

These 3D MIs were calculated for the seven pixelwise kinetic feature map images, generating a 5×7 array of the 3D MIs. Thus, this array of the 3D MIs contain comprehensive information on various aspects of volumetric spatial distribution pattern for each pixelwise kinetic feature. The 5×7 3D MI values are denoted as $M_{21}(V_{S1})$ to $M_4(V_{S1})$, $M_{21}(V_{S2})$ to $M_4(V_{S2})$, $M_{21}(V_{SER})$ to $M_4(V_{SER})$, $M_{21}(V_{PE})$ to $M_4(V_{PE})$, $M_{21}(V_{TTP})$ to $M_4(V_{TTP})$, $M_{21}(V_{W_IS})$ to $M_4(V_{W_IS})$, and $M_{21}(V_{W_OS})$ to $M_4(V_{W_OS})$.

II.E.3. Third level: Extraction of kinetic association features

At the third level, the five kinetic features SER, PE, TTP, W_IS, and W_OS were additionally measured for the time-series of seven spatial features to extract additional information on kinetic association of spatial features within a tumor. At this stage, the seven spatial features were first calculated for the time-series pixelwise TE maps (V_{TE_t}, $0 < t \leq M$), creating additional time-series sets of the spatial features that were not included into the second level feature set. As the number of TEs in data sets 1 and 2 were 4 and 5, respectively, 7×4 spatial feature components were created for data set 1 and 7×5 spatial feature components were created for data set 2. And then, for each time-series set of the seven spatial features, the above five kinetic features were calculated to evaluate the kinetic association of spatial features within a tumor. For example, $PE(\overline{ROI})$ was obtained as the maximum value among the $\overline{ROI}(V_{TE_t})$ ($0 < t \leq M$) and $TTP(\overline{ROI})$ was the time at which the $PE(\overline{ROI})$ occurred. The rationale behind this application is based on the assumption that the kinetic properties evaluated from time-series of spatial features may provide additional information that is not available in spatial features calculated for the pixelwise kinetic feature maps. Thus, a total of 7×5 kinetic feature components were created at the third level: $SER(\overline{ROI})$, $SER(\overline{WT})$, $SER(M_{21})$ to $SER(M_4)$, $PE(\overline{ROI})$, $PE(\overline{WT})$, $PE(M_{21})$ to $PE(M_4)$, $TTP(\overline{ROI})$, $TTP(\overline{WT})$, $TTP(M_{21})$ to $TTP(M_4)$, $W_IS(\overline{ROI})$, $W_IS(\overline{WT})$, $W_IS(M_{21})$ to $W_IS(M_4)$, $W_OS(\overline{ROI})$, $W_OS(\overline{WT})$, and $W_OS(M_{21})$ to $W_OS(M_4)$.

II.F. Predictable values of single features

Our three-level feature extraction procedures produced a total of 7×12 components of spatiotemporal features: 7×7 spatial feature components at the second level and 7×5 kinetic feature components at the third level. While most of these features are spatiotemporal association features that reflect either spatial associations of pixelwise kinetic patterns or kinetic associations of serial spatial properties of tumor enhancements, a subset of them includes relatively simple features that represent only spatial or kinetic aspects of tumor enhancements as most of conventional morphologic or kinetic features do. We selected a set of simple features among our feature array, and used them as references in performance comparison with the spatiotemporal association features. In the second level features, the seven spatial features calculated on V_{S1} were set as simple spatial features, as they represent the spatial properties of only the initial TE image, which are equivalent to conventional form of morphological features. In the third level features, the five kinetic features calculated on only ROI means were set as simple kinetic features, which are the frequently used conventional kinetic features.

The predictable values of each single feature were evaluated by measuring the area under the receiver operating characteristic curve (A_z) using a simple thresholding technique with varying threshold values for the features obtained from all 171 tumor cases. A statistical significance testing was also

performed using a z-test to assess the performance improvement of the spatiotemporal association features over the simple features.[38] In this statistical significance testing, the predictable values were compared among the same kind of features in a pairwise manner between a simple feature and each of its corresponding association features. For example, $M_{21}(V_{S1})$ (simple feature) was compared to each of $M_{21}(V_{S2})$ to $M_{21}(V_{W_OS})$ (association features). The calculation of A_z values and statistical testing for evaluating their difference were performed using MEDCALC statistical software (MED-CALC software version 11.2.1.0, Mariakerke, Belgium).

II.G. Feature selection

Feature selection was performed using a support vector machine-recursive feature elimination (SVM-RFE) algorithm. The SVM-RFE was originally proposed to perform gene selection for cancer classification[39] and was proved to be effective in the selection of an optimal subset of features from a large number of features.[40] This algorithm determines the ranking of each feature based on a sequential backward elimination manner that removes one feature at a time, and searches for a nonlinear separating margin to obtain the optimal hyperplane in the feature space.[41]

In a two-class classification problem, m training samples $\{x_k, y_k\}_{k=1}^m \in \mathfrak{R}^n \times \{-1, 1\}$ consist of the input feature sets x_k and the known class labels y_k. The SVM algorithm first maps the inputs x_k into a high dimensional feature space via a nonlinear mapping function $\varphi(\cdot)$ then computes a decision function of the form[42]

$$g(x) = w^T \varphi(x) + b \tag{19}$$

by maximizing the distance between the set of points $\varphi(x_k)$ to the hyperplane parametrized by the weighted vector w and the bias term b, while being consistent on the training set. The class label of x is obtained by considering the sign of $g(x)$. The learning task in the SVM can be formalized as the following constrained optimization problem:

$$\min_{w, b, \xi} \frac{1}{2} w^T w + C \sum_{k=1}^m \xi_k,$$

$$\text{subject to } y_k g(x_k) \geq 1 - \xi_k, \quad \xi_k \geq 0, \quad \forall k, \tag{20}$$

where C is the regularization parameter, which is a tradeoff between the training accuracy and the prediction term. When C is large, the error term is emphasized. A small C means that the large classification margin is encouraged. ξ is a measure of the number of misclassifications and known as the slack variable. The solution of this problem is obtained using the Lagrangian theory and one can prove that vector w is of the form

$$w = \sum_{k=1}^{N_s} \alpha_k y_k \varphi(x_k), \tag{21}$$

where α_k are the Lagrange multipliers and $\alpha_k > 0$. N_s is the number of training samples x_k which correspond to $\alpha_k > 0$. Vectors x_k for which $\alpha_k > 0$ are called support vectors and the

closest ones to the separating hyperplane. The α_k is the solution of the following quadratic programming (QP) problem:[42]

$$\max_{\alpha} W(\alpha) = \sum_{k=1}^m \alpha_k - \frac{1}{2} \sum_{k,l}^m \alpha_k \alpha_l y_k y_l \left(K(x_k, x_l) + \frac{1}{C} \delta_{k,l} \right),$$

$$\text{subject to } \sum_{k=1}^m y_k \alpha_k = 0 \quad \text{and} \quad \forall k, \quad \alpha_k \geq 0, \tag{22}$$

where $\delta_{k,l}$ is the Kronecker symbol and $K(x_k, x_l) = \varphi(x_k)^T \varphi(x_l)$ is the Gram matrix of the training data. The threshold b is chosen to maximize the margin and is given by

$$b = -\frac{\max_{y_k=-1}(w^T x_k) + \min_{y_k=+1}(w^T x_k)}{2}. \tag{23}$$

The decision function given by the SVM becomes

$$g(x) = w^T \varphi(x) + b = \sum_{k=1}^{N_s} \alpha_k y_k K(x, x_k) + b. \tag{24}$$

We apply the zero-order method for identifying the variable that produces the smallest value of the ranking criterion when removed and use the weight magnitude $\|w\|^2$ as ranking criterion, defined as

$$\|w^{(i)}\|^2 = \sum_{j=1}^{N_s} \sum_{k=1}^{N_s} \alpha_k^{(i)} \alpha_j^{(i)} y_k y_j K^{(i)}(x_k, x_j), \tag{25}$$

where $K^{(i)}$ is the Gram matrix of the training data when the variable i is removed and $\alpha^{(i)}$ is the corresponding solution of the SVM classifier. The rationale of the ranking criterion is that the inputs which are weighted by the largest value have the most influence on the classification decision. Consequently, if the classifier performs well, those inputs with the largest weights correspond to the most informative features. In the implementation of SVM-RFE, we used a radial basis function (RBF) kernel of which $K(x_i, x_j) = \exp(-\|x_i - x_j\|^2 / \sigma^2)$ with $\sigma = 1$ for the nonlinear problem, and set the hyperparameter C to be sufficiently high ($C = 10^3$) in order to keep training error low.

II.H. Tumor differentiation

By using the rank data, we identified several optimal feature sets for use in the final tumor classification. Identification of an optimal feature set was performed by applying a least-squares support vector machine (LS-SVM) classifier to a sequential forward inclusion procedure.[43] The LS-SVM is a modified version of the standard SVM, and is known to be advantageous in handling a large dimensional data and finding an optimal separation based on the limited amount of available training data, without dimensionality reduction.[44]

In principle, LS-SVM simplifies the formulation by replacing the inequality constraint in SVM with an equality constraint. This approach significantly reduces the cost in complexity and computation time, solving a set of linear

equations instead of solving the QP problem. The LS-SVM algorithm considers the following constrained optimization problem:[45]

$$\min_{w,b,e} \frac{1}{2} w^T w + \frac{1}{2} \gamma \sum_{k=1}^{m} e_k^2,$$

subject to the equality constraints $y_k = g(x_k)$

$$+ e_k, \quad \forall k, \tag{26}$$

where γ is a regularization parameter controlling the bias-variance tradeoff and e_k are normal distributed errors of the outputs y_k. The solution is considered in the dual form of Eq. (26), which is given by the following set of linear equations:[45]

$$\begin{bmatrix} K + \gamma^{-1} I_m & 1_v \\ 1_v^T & 0 \end{bmatrix} \begin{bmatrix} \alpha \\ b \end{bmatrix} = \begin{bmatrix} y \\ 0 \end{bmatrix}, \tag{27}$$

where $y = [y_1; \cdots; y_m]$, $\alpha = [\alpha_1; \cdots; \alpha_m]$, $1_v = [1; \cdots; 1]$, $K_{ij} = K(x_i, x_j)$, and I_m is the identity matrix of size m. Equation (27) can be factorized into the form a positive definite system

$$\begin{bmatrix} H & 0 \\ 0 & 1_v^T H^{-1} 1_v \end{bmatrix} \begin{bmatrix} \alpha + H^{-1} 1_v b \\ b \end{bmatrix} = \begin{bmatrix} y \\ 1_v^T H^{-1} y \end{bmatrix}, \tag{28}$$

with $H = K + \gamma^{-1} I_m$. Since $1_v^T H^{-1} 1_v > 0$ is positive and H is positive definite, the overall matrix is also positive definite. The model parameters α and b can be obtained in terms of H^{-1} by

$$\alpha = H^{-1}(y - b1_v), \tag{29}$$

$$b = 1_v H^{-1} y (1_v^T H^{-1} 1_v)^{-1}. \tag{30}$$

The decision function given by the LS-SVM becomes

$$g(x) = w^T \varphi(x) + b = \sum_{k=1}^{m} \alpha_k y_k K(x, x_k) + b. \tag{31}$$

In the implementation of the LS-SVM algorithm, a RBF kernel of which $K(x_i, x_j) = \exp(-\|x_i - x_j\|^2 / \sigma^2)$ was used for classification. In this configuration, two hyperparameters (σ, γ) have to be determined. Each time LS-SVM was trained with a feature set selected from the ranked features, the hyperparameters σ, γ were initialized with randomized values and tuned to optimal values by grid search after applying the algorithm to the Ripley's synthetic data set generated from mixtures of two Gaussian distributions.[46] In the sequential forward inclusion procedure, the top ranked feature was first selected at an initial state, and then each feature was added to the previously selected feature set at a time in order given by the rank data set, and the performance of a new feature set was tested by the LS-SVM. An optimal feature set was determined as the feature set which recorded the best classification performance during the sequential forward inclusion procedure. This procedure was repeated three times to find an optimized simple feature set which was determined by using only simple form features, an optimized second

level feature set which was determined by using only second level features, and an optimized second and third level feature set which was determined by using all second and third level features. In order to obtain reliable performance, the leave-one-out test was performed. Area under the ROC curve (A_z) was used as a performance measure in the binary classification of malignant and benign tumors. For comparison of A_z values of SVM classifiers using different features, their standard errors and statistical significances (p-values) were calculated by using MEDCALC statistical software according to the way described by Hanley and McNeil.[38]

III. RESULTS

III.A. Distribution of second and third level features

The box plots in Figs. 7(a)–7(f) compare the distributions of the selected spatiotemporal feature values for malignant and benign tumors. The base-10 logarithmic values of features are displayed for convenience of visual presentation because of large variations in their distribution range. Figures 7(a)–7(c) show the distributions of three spatial features [i.e., $\overline{\text{WT}}(\cdot)$, $M_{21}(\cdot)$, and $M_{23}(\cdot)$] for seven pixelwise kinetic feature maps. In general, the feature values significantly overlap in their distributions between malignant and benign cases regardless of whether they are simple or association types. However, it is noteworthy that the TTP map-based spatial features [i.e., $\overline{\text{WT}}(V_{\text{TTP}})$, $M_{21}(V_{\text{TTP}})$, and $M_{23}(V_{\text{TTP}})$] maintain relatively consistent distinction between malignant and benign tumors. Shown in Figs. 7(d)–7(f) are the distributions of $\text{SER}(\cdot)$, $\text{W}_{\text{I}}\text{S}(\cdot)$, and $\text{W}_{\text{O}}\text{S}(\cdot)$, evaluated for the time-series of seven spatial features, respectively. In those kinetic features, the level of distinction does not vary much upon the types of spatial features from which they were extracted, although those of $\overline{\text{ROI}}$ and $\overline{\text{WT}}$ show slightly higher differences.

III.B. Predictable values

Table III shows the predictable values of each single feature in our multilevel feature array. Among the second level features, $\overline{\text{ROI}}(V_{\text{TTP}})$, $M_{22}(V_{\text{TTP}})$, and $M_{23}(V_{\text{TTP}})$ were the most predictable ones having A_z of 0.75, which compare to $\overline{\text{ROI}}(V_{S1})$ having A_z of 0.69, the most predictable simple feature in the second level. It is noteworthy that there were significant improvements in predictable values of $M_{22}(V_{\text{TTP}})$ and $M_{23}(V_{\text{TTP}})$, which taking account of spatial association of pixelwise kinetic feature maps, over their simple forms [i.e., $M_{22}(V_{S1})$ and $M_{23}(V_{S1})$], both having A_z of 0.54. Also shown as statistically significant improvement over their simple forms were $M_{21}(V_{\text{TTP}})$, $M_{22}(V_{S2})$, $M_{23}(V_{S2})$, $M_{23}(V_{\text{PE}})$, $M_3(V_{\text{TTP}})$, $M_3(V_{\text{W}_\text{I}\text{S}})$, $M_3(V_{\text{W}_\text{O}\text{S}})$, and $M_4(V_{\text{TTP}})$. Overall, the V_{TTP}-based features ranked top range of predictable values (0.62–0.75), while V_{PE}-based features ranked bottom range (0.52–0.59). Among the third level features, three $\overline{\text{ROI}}$-based kinetic features [i.e., $\text{SER}(\overline{\text{ROI}})$, $\text{TTP}(\overline{\text{ROI}})$, $\text{W}_\text{I}\text{S}(\overline{\text{ROI}})$, and $\text{TTP}(\overline{\text{WT}})$] were in top ranks having A_z of
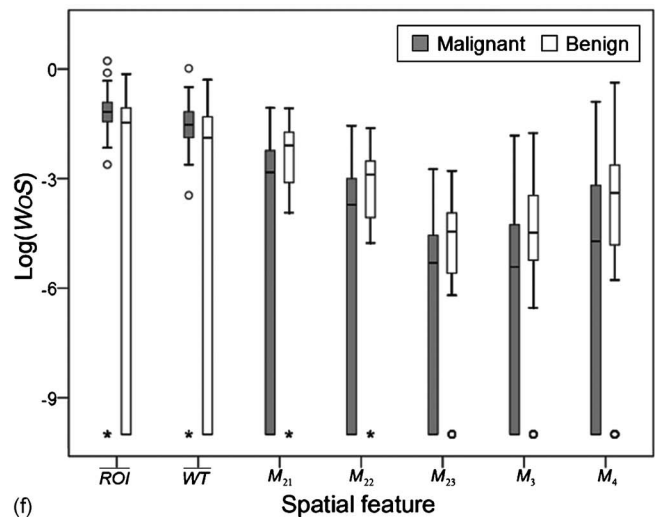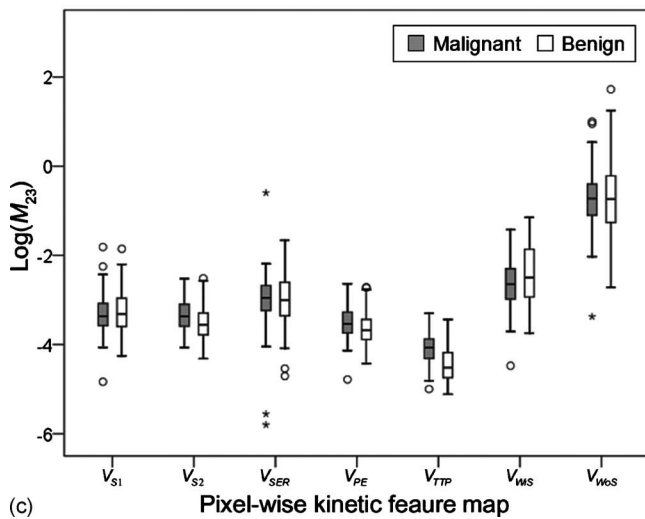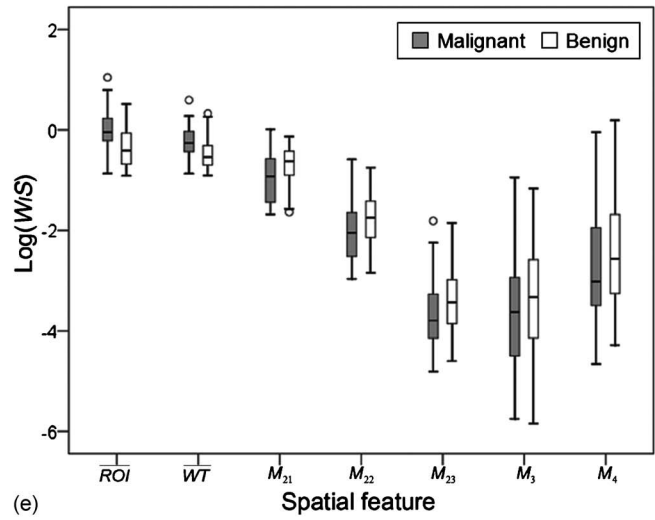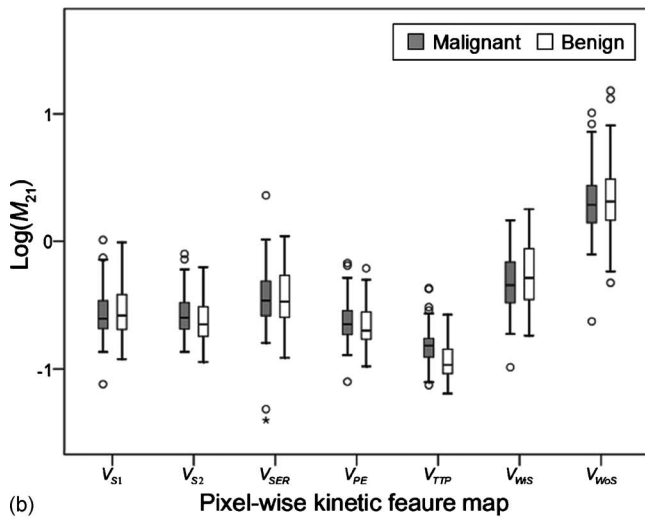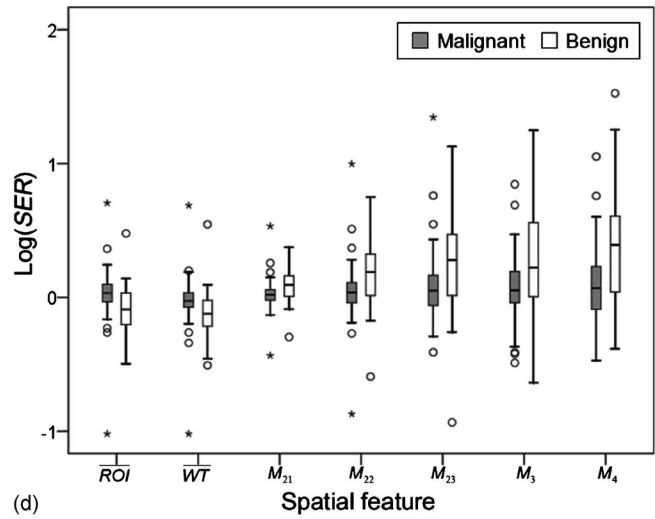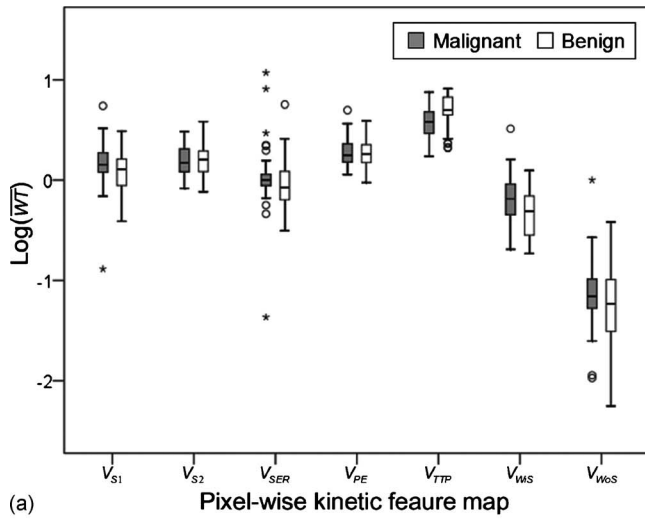
FIG. 7. Box plots representing distributions of selected spatial and kinetic association features. Distributions of three spatial association features such as (a) mean WT, (b) M_{21}, and (c) M_{23} are shown for each pixelwise kinetic feature map. Distributions of kinetic association features (SER, W_IS, and W_OS) are shown in (d)–(f) for seven spatial features, respectively. Gray bars are for malignant tumors and white bars are for benign tumors. Base-10 log transformation was used for convenience of visual presentation. The boundaries of the box indicate the 25th and 75th percentiles and the horizontal bar inside the box represents the median value. Lines are drawn from both ends of the box to denote the largest and smallest values. The outliers (o) and extreme values (*) are those with magnitudes between 1.5 and 3 box lengths and more than 3 box lengths, respectively.

TABLE III. Predictable values for tumor differentiation in single features as represented by A_z values in the ROC analysis. Italic sections in the second and third level feature set represent a subset of simple form features which do not reflect spatiotemporal association.

Spatial feature	Second level feature set							Third level feature set				
	V_{S1}	V_{S2}	V_{SER}	V_{PE}	V_{TTP}	V_{W_IS}	V_{W_OS}	SER	PE	TTP	W_IS	W_OS
$\overline{ROI}$	*0.69*	*0.51*	*0.69*	*0.58*	*0.75*	*0.72*	*0.66*	*0.74*	*0.58*	*0.73*	*0.73*	*0.66*
$\overline{WT}$	0.65	0.52	0.62	0.52	0.72	0.68	0.61	0.70	0.51	0.73	0.71	0.62
M_{21}	*0.53*	0.59	0.50	0.57	$\mathbf{0.73^a}$	0.57	0.51	0.69	0.53	0.66	0.64	0.71
M_{22}	*0.54*	$\mathbf{0.60^a}$	0.50	0.58	$\mathbf{0.75^a}$	0.57	0.50	0.70	0.53	0.65	0.63	0.70
M_{23}	*0.54*	$\mathbf{0.62^a}$	0.50	$\mathbf{0.59^a}$	$\mathbf{0.75^a}$	0.58	0.51	0.70	0.53	0.65	0.62	0.69
M_3	*0.53*	0.54	0.54	0.53	$\mathbf{0.62^a}$	$\mathbf{0.56^a}$	$\mathbf{0.60^a}$	0.66	0.53	0.62	0.56	0.66
M_4	*0.54*	0.56	0.51	0.54	$\mathbf{0.69^a}$	0.57	0.55	0.70	0.54	0.65	0.59	0.66

[a]Indicate a statistically significant improvement ($p < 0.05$) over their corresponding simple form features.

0.73–0.74. Unlike the case of the second level features, the performance improvement of kinetic association features over simple features was not observed.

III.C. Optimized feature sets

Our feature selection procedure identified three optimized feature sets: An optimized simple feature set, $[M_{21}(V_{S1})$, $SER(\overline{ROI})$, $\overline{WT}(V_{S1})$, $PE(\overline{ROI})$, $W_OS(\overline{ROI})$, $M_{22}(V_{S1})$, $W_IS(\overline{ROI})$, $M_{23}(V_{S1})$, and $\overline{ROI}(V_{S1})]$; an optimized second level feature set, $[\overline{ROI}(V_{TTP})$, $\overline{WT}(V_{TTP})$, $M_{21}(V_{S2})$, and $M_{21}(V_{W_OS})]$; and an optimized second and third level feature set, $[M_{23}(V_{PE})$, $\overline{WT}(V_{TTP})$, $\overline{WT}(V_{S2})$, $\overline{WT}(V_{S1})$, $SER(M_{21})$, $W_OS(\overline{WT})$, $W_IS(\overline{WT})$, and $M_{21}(V_{W_OS})]$. In Figs. 8(a) and 8(b), the distributions of feature values from the optimized simple feature set and the optimized second and third level feature set are depicted in 2D scatter plots with their two principal component values. The projection on to the principal component axes was performed using SPSS statistics software package (SPSS for windows 16.0, Inc. 1989–2007, Chicago, IL). The malignant cases are denoted with black circles and benign cases with white circles. In the scatter plot of Fig. 8(a), there was a considerable overlap between malignant and benign cases in the distributions of the first and second

principal component values from the optimized simple feature set. On the other hand, the scatter plot in Fig. 8(b) shows substantially improved distinction between malignant and benign cases in the distribution of the two principal component values from the optimized second and third level feature set.

III.D. Tumor differentiation performance

The tumor differentiation performances of our selected features as evaluated with leave-one-out A_z values using a LS-SVM classifier are summarized in Table IV. The leave-one-out A_z values of two single features, $SER(\overline{ROI})$ (best single simple feature) and $\overline{ROI}(V_{TTP})$ (best single association feature), shown as references were 0.68 and 0.74, respectively. The highest performance among all feature sets were shown with the optimized second and third level feature set to have A_z of 0.88, whereas the optimized second level feature set showed a little lower performance ($A_z = 0.84$), although the difference was not statistically significant ($p = 0.21$). The A_z of the optimized simple feature set was 0.79, which was lowest among the three optimized feature sets, although it was significantly higher over the best single simple feature. Note that the performance differences neither

TABLE IV. Comparison of performances among different optimal feature sets as evaluated with leave-one-out A_z of LS-SVM classifier. Performances of two single features (best single simple feature and best single association feature) were shown as references. p-values represent statistical significance of performance differences between each pair of feature sets as evaluated using a z-test.

Feature		A_z (mean $\pm$ 1.96 SE)	p-value	Sensitivity (%)	Specificity (%)
Best single simple feature	$SER(\overline{ROI})$	0.68 ± 0.07		95	47
Best single association feature	$\overline{ROI}(V_{TTP})$	0.74 ± 0.07		89	53
Optimized simple feature set	$M_{21}(V_{S1})$, $SER(\overline{ROI})$, $\overline{WT}(V_{S1})$, $PE(\overline{ROI})$, $W_OS(\overline{ROI})$, $M_{22}(V_{S1})$, $W_IS(\overline{ROI})$, $M_{23}(V_{S1})$, $\overline{ROI}(V_{S1})$	0.79 ± 0.06	0.25 / 0.014[a]	73	78
Optimized second level feature set	$\overline{ROI}(V_{TTP})$, $\overline{WT}(V_{TTP})$, $M_{21}(V_{S2})$, $M_{21}(V_{W_OS})$	0.84 ± 0.06	0.21	87	73
Optimized second and third level feature set	$M_{23}(V_{PE})$, $\overline{WT}(V_{TTP})$, $\overline{WT}(V_{S2})$, $\overline{WT}(V_{S1})$ $SER(M_{21})$, $W_OS(\overline{WT})$, $W_IS(\overline{WT})$, $M_{21}(V_{W_OS})$	0.88 ± 0.05		76	88

[a]Indicates statistically significant difference ($p < 0.05$).

Optimized simple feature set

(a)

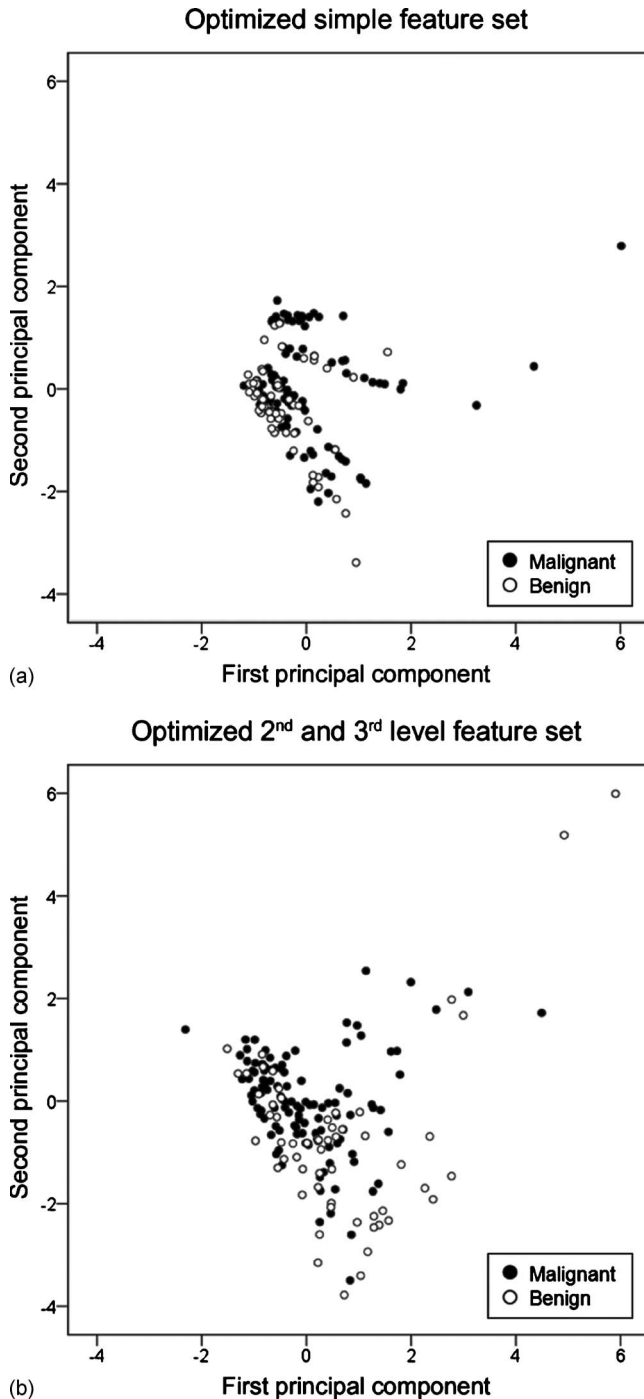## Optimized 2ⁿᵈ and 3ʳᵈ level feature set

(b)

FIG. 8. 2D scatter plots compare the distributions of first and second principal component values for the tumor cases taken from (a) the optimized simple feature set and (b) optimized second and third level feature set. White circles denote benign cases and black circles denote malignant cases. Note that there was a significant overlap between malignant and benign tumors in the distribution of two principal component values in (a), whereas a substantially improved distinction is noticed between malignant and benign tumors in the distribution of two principal component values in (b).

between the optimized simple feature set and the optimized second level feature set nor between the optimized second level feature set and the optimized second and third level feature set were statistically significant ($p = 0.25$ and 0.21),

whereas improvement of the optimized second and third level feature set over the optimized simple feature set was statistically significant ($p = 0.014$).

The ROC curves of the two best single features and three optimized feature sets were depicted in Fig. 9. The smooth ROC curves were plotted using JROCFIT.[47] The optimized second and third level feature set shows the highest sensitivity at most specificity levels over the other features, followed by the optimized second level feature set, optimized simple feature set, best single association feature $[\overline{\text{ROI}}(V_{\text{TTP}})]$, and best single simple feature $[\text{SER}(\overline{\text{ROI}})]$.

Figure 10 shows the changes of classification accuracy (A_z) of LS-SVM according to the number of features included in order, as ranked by SVM-RFE from the combined second and third level features. The accuracy increases abruptly up to its highest peak at the number 8, and then shows a decreasing tendency along with some fluctuations later on. This suggests that the redundant features have to be identified and eliminated in order to yield a best classification performance and that how to determine the ranks of each feature should be chosen carefully.

IV. DISCUSSION

IV.A. Postulate of this study

Breast DCE-MRI represents the challenges faced in radiological interpretation of multidimensional imaging data today. Dynamic 3D images are produced during the time course of contrast enhancement, which contain rich information involving functional and anatomical aspects of breast tissues. However, capturing and interpreting of complex spatiotemporal signal patterns in such dynamic 3D images in everyday practices surpass human ability. This mismatch between the efficiencies of image production and interpretation often causes intraobserver and interobserver variability in diagnostic performance and makes a bottleneck in diagnostic workflow as well in breast DCE-MRI.[48] Therefore, the motivation of this study was to develop a CAD scheme that can effectively characterize such spatiotemporal signal patterns of tumor enhancement in multidimensional image data set in DCE-MRI.

In this study, we postulated that analyzing spatiotemporal association would provide additional information on tumor differentiation that was not attainable using conventional approaches in which spatial or temporal features were extracted separately. Based on this postulation, we presented a novel approach to breast MRI CAD using a multilevel analysis of spatiotemporal association features for tumor enhancement patterns in DCE-MRI. Spatial association features (second level features) for pixelwise kinetic patterns as well as kinetic association features (third level features) for time-series of spatial features were extracted in the proposed multilevel feature extraction procedure.

IV.B. Testing of postulate

In order to test our postulate, we first evaluated the performance improvements of our spatiotemporal association

features over the conventional approach at a single feature level. In a statistical test comparing the predictable values of association features with that of their corresponding simple form feature, ten out of 72 association features were found to show statistically significant improvements. Noteworthy were the 3D MI features which exhibited up to 21% increase in their mean predictable values. These results suggest that our multilevel feature extraction procedures were able to condense more compact information at a single feature level. None of single features, however, showed sufficient accuracy in tumor differentiation. The performance of the best single feature [i.e., $\overline{\text{ROI}}(V_{\text{TTP}})$] as evaluated with leave-one-out A_z remained 0.74. Also, diverse levels of the predictable value for each feature shown in Table III appear to reveal the fact that the characteristic information on tumor enhancements are scattered in various forms of spatial and temporal signal patterns in 4D signal space, as we postulated.

Next, we evaluated the performance improvements of the optimized feature sets. Best performance was shown in the optimized second and third level feature set to have A_z of 0.88, which was a substantial improvement over the best single feature (0.88 vs 0.74, $p < 0.002$). This feature set also showed a statistically significant performance improvement over the optimized simple feature set (0.88 vs 0.79, $p < 0.05$). It is interesting to note that none of simple features except for $\overline{\text{WT}}(V_{S1})$ were included in the optimized second and third level feature set, although all simple features were allowed to be included together with the association features in feature selection process. Also of note is the fact that the optimized second level feature set did not show significant improvement over the optimized simple feature set; both sec-

ond and third level features were necessary to achieve a significant performance improvement. This indicates that our second and third level spatiotemporal association features capture different parts of information scattered in 4D signal space of tumor enhancements. These results appear to support our postulate that analyzing spatiotemporal association of tumor enhancement patterns would gain additional information, which in turn may lead to improved tumor differentiation as compared to the conventional way using spatial and temporal features separately.

IV.C. 3D moment invariants

Comparing our performance results with those of previous breast MRI CAD studies,[17,19,20] in which A_z values ranged from 0.74 to 0.97, the performance of our developed CAD scheme appears to be in high range. We attribute the relatively good performance of the proposed CAD scheme in part to the employment of 3D MI descriptors for spatial feature extraction. The 3D MI-based features constituted three out of eight features in the optimized second and third level feature set, which is a considerable proportion.

The 3D MIs have been shown to successfully characterize spatial distribution of functional MRI activations.[37] However, to the knowledge of the authors, it was for the first time that 3D MIs were used for extraction of spatial features on tumor enhancement patterns in this study. Margin characteristic and contour irregularity have been reported as the most predictable architectural feature in many studies.[8,49] Another importantly reported morphological predictor was an area enhancement or internal enhancement distribution,[8] suggesting that regional, clumped, or rim enhancements are strongly associated with malignancy. To include morphological feature in CAD, Gilhuijs *et al.*[18] measured radial gradient histogram and margin gradient and Meinel *et al.*[20] calculated standard deviation of radial length and compactness for seg-
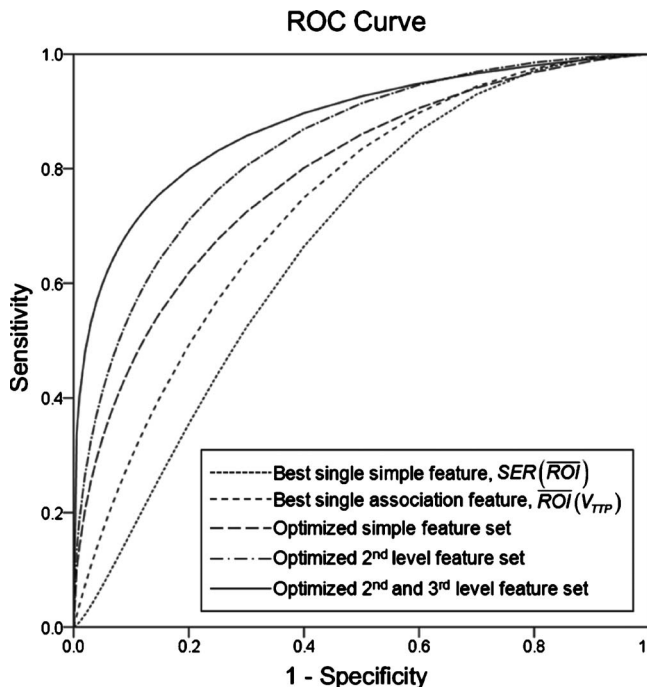

FIG. 9. ROC curves compare the classification performances of the three optimized feature sets, along with those of the two single features. A leave-one-out testing was used to evaluate the ROC performances.
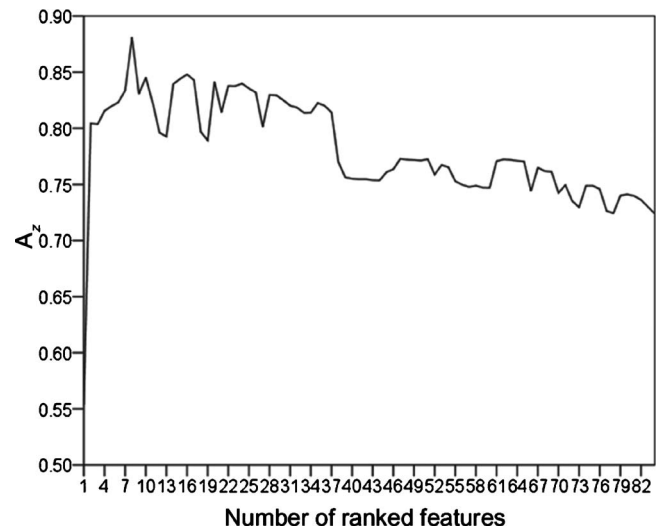

FIG. 10. A plot shows the trends of classification accuracy (A_z) of LS-SVM classifier according to the number of included features in order as ranked by SVM-RFE algorithm. The combined second and third level features are used in feature ranking.

mented tumors. While these descriptors were useful to capture boundary characteristics of the segmented tumor, they are unable to evaluate the area enhancement or internal enhancement distribution which require to describe the spatial distribution of tumor enhancements on a continuous tone image. The 3D MIs used in this study extract multiple orders of 3D spatial moments on continuous tone volumetric images, and thus are able to describe internal enhancement as well as to characterize 3D morphological patterns within a tumor. The results of our study appear to show that 3D MIs are able to successfully characterize the morphological aspects of tumor enhancements in breast DCE-MRI.

IV.D. FCM segmentation

In the application of automated feature classification technique to tumor differentiation, the performance depends significantly on appropriate tumor segmentation.[22] In previous breast MRI CAD studies, tumor segmentation was frequently done manually, which suffers intraobserver and interobserver variability. In this study, we applied an automated tumor segmentation technique in order to obtain more reliable performance measure free from user's manual intervention. We employed a FCM clustering approach, which has been often recommended for the segmentation of a tumor in breast DCE-MRI.[24,25] In our realization, we extracted a scalar value (i.e., VES) at each pixel and used it in FCM clustering. The VES used in this study takes a modified form of the weighted variance which was proposed by Alderliesten *et al.*[26] for increasing the conspicuity of tumors against slowly enhancing surrounding parenchyma. Although a scalar value-based FCM approach was used considering two different time-series protocols of MRI data in this study, there are studies using FCM clustering technique that takes all time-series signals as inputs to create segmentation membership. Selecting different types of FCM clustering technique and determining optimal parameters such as the segmentation threshold may lead to differences in tumor classification performance, which is an interesting research subject. However, it was out of the scope of this study. That issue remains as a further study.

IV.E. Image registration

There are still several limitations in this study. First, we applied 3D rigid registration technique to correct possible patient motions during acquisitions of MR data. In literatures, nonrigid registration techniques were shown to improve the accuracy of tumor segmentation and tissue alignment in case of significant motion artifacts.[50,51] However, we were concerned about the risk of local misalignment within a tumor that might be introduced by the nonrigid registration procedure due to the confusion between rapid kinetic changes and patient motion. Actually, a previous breast MRI CAD study comparing the various registration techniques reported that a CAD scheme with a rigid image registration yielded the best performance in tumor differentiation among various registration options.[52] It would be an interesting re-search topic to investigate the effect of the nonrigid registration on improvement in tumor differentiation performance of a CAD scheme.

TABLE V. Comparison of performances between data sets 1 and 2 as evaluated with leave-one-out A_z. The same LS-SVM classifier and the optimized second and third level feature set were used for both data sets.

Data set	A_z (mean $\pm$ 1.96 SE)	p-value	Sensitivity (%)	Specificity (%)
Data set 1	0.90 ± 0.08	0.614	82	88
Data set 2	0.87 ± 0.07		92	72

IV.F. Ability to generalize

Second, the data sets we used were obtained with two protocols each using different MRI machines. Therefore, some of our methods have to be compromised to be applicable to both data sets, which might have limited the performance improvement. Ideally, use of a best combination of an imaging protocol and CAD scheme in both development stages and clinical applications would bring a highest possible performance. In reality, however, use of diverse acquisition protocols and different MRI machines are unavoidable across different institutions. Even at the same institution, system replacement or upgrade may cause changes of acquisition protocols. Therefore, development of a CAD scheme with data sets consisting of different protocols as done in this study may better reflect real-world cases. In this scenario, finding a way to tune techniques to be applicable to different data sets and thereby to yield a robust output would determine the level of generalizability of the developed CAD scheme.

In this study, we chose a set of kinetic features at the first level for the feature extraction that carry a common meaning despite the differences of temporal acquisition protocols. The scale normalization process of 3D MIs also made them robust to the differences of spatial resolution in two data sets. Use of VES in FCM clustering also contributed to the robustness of our CAD scheme. In a preliminary experiment to test the generalizability of our CAD scheme, the performance results were shown to be similar for the two data sets (0.90 vs 0.87, $p > 0.60$) as shown in Table V. Therefore, although our CAD scheme might have sacrificed some fraction of performance, it appears to represent a robust and generalizable CAD scheme to different protocols in breast DCE-MRI. In this regard, however, a further study will be necessary to validate the generalizability of our CAD scheme that includes more patient cases and participation of multiple institutions.

IV.G. Other limitations

Third, there was no observer performance evaluation. The CAD is, by definition, for effective assistance of human observer's interpretation. Accordingly, the final value of any CAD scheme has to be determined in terms of observer per-

formance improvements. Therefore, an observer performance study is warranted to finally judge the value of our developed CAD scheme.

Finally, this study presented a multilevel feature extraction approach to analyzing the spatiotemporal association of tumor enhancement patterns. Although our method showed a promising performance results, it was one of many possible approaches. An extended study to explore further potentials of analyzing the spatiotemporal association of tumor enhancement patterns will be a challenging and yet valuable task to advance CAD techniques to find a more essential role in future applications.

V. CONCLUSION

This work presented a novel approach to breast MRI CAD based on multilevel analysis of spatiotemporal association features in tumor enhancement patterns. The spatiotemporal association features derived by our multilevel analysis strategy were shown to collect various aspects of characteristic tumor information effectively. By optimizing a feature set using these spatiotemporal association features and classifying with LS-SVM, a high performance tumor classification was possible, achieving A_z of 0.88.

Comparing with a feature set which does not reflect the spatiotemporal association, our multilevel feature analysis strategy showed a statistically significant performance improvement ($p < 0.05$). Our proposed CAD framework has a potential for improving diagnostic performance in breast DCE-MRI.

ACKNOWLEDGMENTS

[a]Author to whom correspondence should be addressed. Electronic mail: kimjhyo@snu.ac.kr

[b]Present address: Department of Radiology, Hanyang University College of Medicine, Seoul 133-791, Korea.

[1]M. J. Stoutjesdijk, C. Boetes, G. J. Jager, L. Beex, P. Bult, J. H. Hendriks, R. J. Laheij, L. Massuger, L. E. van Die, T. Wobbes, and J. O. Barentsz, "Magnetic resonance imaging and mammography in women with a hereditary risk of breast cancer," J. Natl. Cancer Inst. **93**, 1095–1102 (2001).

[2]L. Liberman, "Breast cancer screening with MRI—What are the data for patients at high risk?," N. Engl. J. Med. **351**, 497–500 (2004).

[3]C. K. Kuhl, S. Schrading, C. C. Leutner, N. Morakkabati-Spitz, E. Wardelmann, R. Fimmers, W. Kuhn, and H. H. Schild, "Mammography, breast ultrasound, and magnetic resonance imaging for surveillance of women at high familial risk for breast cancer," J. Clin. Oncol. **23**, 8469–8476 (2005).

[4]M. O. Leach, C. R. Boggis, A. K. Dixon, D. F. Easton, R. A. Eeles, D. G. Evans, F. J. Gilbert, I. Griebsch, R. J. Hoff, P. Kessar, S. R. Lakhani, S. M. Moss, A. Nerurkar, A. R. Padhani, L. J. Pointon, D. Thompson, R. M. Warren (MARIBS Study Group), "Screening with magnetic resonance imaging and mammography of a UK population at high risk of breast cancer: A prospective multicentre cohort study (MARIBS)," Lancet **365**, 1769–1778 (2005).

[5]F. Sardanelli, F. Podo, G. D'Agnolo, A. Verdecchia, M. Santaguilani, R. Musumeci, G. Trecate, S. Manoukian, S. Morassut, C. de Giacomi, M. Federico, L. Cortesi, S. Corcione, S. Cirillo, V. Marra (High Breast Cancer Risk Italian Trial), A. Cilotti, C. Di Maggio, A. Fausto, L. Preda, C. Zuiani, A. Contegiacomo, A. Orlacchio, M. Calabrese, L. Bonomo, E. Di Cesare, M. Tonutti, P. Panizza, and A. Del Maschio, and the , "Multicenter comparative multimodality surveillance of women at genetic-familial high risk for breast cancer (HIBCRIT): Interim results," Radiology **242**, 698–715 (2007).

[6]M. O. Leach, "Breast cancer screening in women at high risk using MRI," NMR Biomed. **22**, 17–27 (2009).

[7]T. C. Williams, W. B. DeMartini, S. C. Partridge, S. Peacock, and C. D. Lehman, "Breast MR imaging: Computer-aided evaluation program for discriminating benign from malignant lesions," Radiology **244**, 94–103 (2007).

[8]M. D. Schnall, J. Blume, D. A. Bluemke, G. A. DeAngelis, N. DeBruhl, S. Harms, S. H. Heywang-Kobrunner, N. Hylton, C. K. Kuhl, E. D. Pisano, P. Causer, S. J. Schnitt, D. Thickman, C. B. Stelling, P. T. Weatherall, C. Lehman, and C. A. Gatsonis, "Diagnostic architectural and dynamic features at breast MR imaging: Multicenter study," Radiology **238**, 42–53 (2006).

[9]C. K. Kuhl, P. Mielcareck, S. Klaschik, C. Leutner, E. Wardelmann, J. Gieseke, and H. H. Schild, "Dynamic breast MR imaging: Are signal intensity time course data useful for differential diagnosis of enhancing lesions?," Radiology **211**, 101–110 (1999).

[10]O. Ikeda, R. Nishimura, H. Miyayama, T. Yasunaga, Y. Ozaki, A. Tuji, and Y. Yamashita, "Evaluation of tumor angiogenesis using dynamic enhanced magnetic resonance imaging: Comparison of plasma vascular endothelial growth factor, hemodynamic, and pharmacokinetic parameters," Acta Radiol. **45**, 446–452 (2004).

[11]L. W. Nunes, M. D. Schnall, and S. G. Orel, "Update of breast MR imaging architectural interpretation model," Radiology **219**, 484–494 (2001).

[12]U. Wedegärtner, U. Bick, K. Wortler, E. Rummerny, and G. Bongartz, "Differentiation between benign and malignant findings on MR-mammography: Usefulness of morphological criteria," Eur. Radiol. **11**, 1645–1650 (2001).

[13]U. S. G. Orel, "Differentiating benign from malignant enhancing lesions identified at MR imaging of the breast: Are time signal-intensity curves an accurate predictor?," Radiology **211**, 5–7 (1999).

[14]S. Mussurakis, D. L. Buckley, and A. Horsman, "Dynamic MRI of invasive breast cancer: Assessment of three region-of-interest analysis methods," J. Comput. Assist. Tomogr. **21**, 431–438 (1997).

[15]*ACR BI-RADS-MRI*, 1st ed. (American College of Radiology, Reston, VA, 2003).

[16]R. E. Lucht, M. V. Knopp, and G. Brix, "Classification of signal-time curves from dynamic MR mammography by neural networks," Magn. Reson. Imaging **19**, 51–57 (2001).

[17]J. Levman, T. Leung, P. Causer, D. Plewes, and A. L. Martel, "Classification of dynamic contrast-enhanced magnetic resonance breast lesions by support vector machines," IEEE Trans. Med. Imaging **27**, 688–696 (2008).

[18]K. G. Gilhuijs, M. L. Giger, and U. Bick, "Computerized analysis of breast lesions in three dimensions using dynamic magnetic-resonance imaging," Med. Phys. **25**, 1647–1654 (1998).

[19]W. Chen, M. L. Giger, L. Lan, and U. Bick, "Computerized interpretation of breast MRI: Investigation of enhancement-variance dynamics," Med. Phys. **31**, 1076–1082 (2004).

[20]L. A. Meinel, A. H. Stolpen, K. S. Berbaum, L. L. Fajardo, and J. M. Reinhardt, "Breast MRI lesion classification: Improved performance of human readers with a backpropagation neural network computer-aided diagnosis (CAD) system," J. Magn. Reson Imaging **25**, 89–95 (2007).

[21]Y. Zheng, S. Englander, M. D. Schnall, and D. Shen, "STEP: Spatial-temporal enhancement pattern, for MR-based breast tumor diagnosis," in *Proceedings of the Fourth IEEE International Symposium on Biomedical Imaging: From to Nano to Macro*, 2007 (IEEE, New York, 2007), pp. 520–523.

[22]Y. Zheng, S. Englander, S. Baloch, E. I. Zacharaki, Y. Fan, M. D. Schnall, and D. Shen, "STEP: Spatiotemporal enhancement pattern for MR-based breast tumor diagnosis," Med. Phys. **36**, 3192–3204 (2009).

[23]W. M. Wells III, P. Viola, H. Atsumi, S. Nakajima, and R. Kikinis, "Multi-modal volume registration by maximization of mutual information," Med. Image Anal. **1**, 35–51 (1996).

[24]W. Chen, M. L. Giger, and U. Bick, "A fuzzy c-means (FCM)-based approach for computerized segmentation of breast lesions in dynamic contrast-enhanced MR images," Acad. Radiol. **13**, 63–72 (2006).

[25]J. Shi, B. Sahiner, H. P. Chan, C. Paramagul, L. M. Hadjiiski, M. Helvie, and T. Chenevert, "Treatment response assessment of breast masses on dynamic contrast-enhanced magnetic resonance scans using fuzzy c-means clustering and level set segmentation," Med. Phys. **36**, 5052–5063 (2009).

[26]T. Alderliesten, A. Schlief, J. Peterse, C. Loo, H. Teertstra, S. Muller, and K. Gilhuijs, "Validation of semiautomatic measurement of the extent of breast tumors using contrast-enhanced magnetic resonance imaging," Invest. Radiol. **42**, 42–49 (2007).

[27]H. Degani, V. Gusis, D. Weinstein, S. Fields, and S. Strano, "Mapping pathophysiological features of breast tumors by MRI at high spatial resolution," Nat. Med. **3**, 780–782 (1997).

[28]N. M. Hylton, "Vascularity assessment of breast lesions with gadolinium-enhanced MR imaging," Magn. Reson Imaging Clin. N. Am. **9**, 321–332 (2001).

[29]K. L. Li, R. G. Henry, L. J. Wilmes, J. Gibbs, X. Zhu, Y. Lu, and N. M. Hylton, "Kinetic assessment of breast tumors using high spatial resolution signal enhancement ratio (SER) imaging," Magn. Reson. Med. **58**, 572–581 (2007).

[30]E. Furman-Haran, D. Grobgeld, R. Margalit, and H. Degani, "Response of MCF7 human breast cancer to tamoxifen: Evaluation by the three-time-point, contrast-enhanced magnetic resonance imaging method," Clin. Cancer Res. **4**, 2299–2304 (1998).

[31]E. Furman-Haran, D. Grobgeld, F. Kelcz, and H. Degani, "Critical role of spatial resolution in dynamic contrast-enhanced breast MRI," J. Magn. Reson Imaging **13**, 862–867 (2001).

[32]F. Kelcz, E. Furman-Haran, D. Grobgeld, and H. Degani, "Clinical testing of high-spatial-resolution parametric contrast-enhanced MR imaging of the breast," AJR, Am. J. Roentgenol. **179**, 1485–1492 (2002).

[33]S. Mussurakis, D. L. Buckley, and A. Horsman, "Dynamic MR imaging of invasive breast cancer: Correlation with tumour grade and other histological factors," Br. J. Radiol. **70**, 446–451 (1997).

[34]G. P. Liney, P. Gibbs, C. Hayes, M. O. Leach, and L. W. Turnbull, "Dynamic contrast-enhanced MRI in the differentiation of breast tumors: User-defined versus semi-automated region-of-interest analysis," J. Magn. Reson Imaging **10**, 945–949 (1999).

[35]P. A. Baltzer, D. M. Renz, P. E. Kullnig, M. Gajda, O. Camara, and W. A. Kaiser, "Application of computer-aided diagnosis (CAD) in MR-mammography (MRM): Do we really need whole lesion time curve distribution analysis?," Acad. Radiol. **16**, 435–442 (2009).

[36]F. A. Sadjadi and E. L. Hall, "Three-dimensional moment invariants," IEEE Trans. Pattern Anal. Mach. Intell. **PAMI-2**, 127–136 (1980).

[37]B. Ng, R. Abugharbieh, X. Huang, and M. J. McKeown, "Spatial characterization of fMRI activation maps using invariant 3D moment descriptors," IEEE Trans. Med. Imaging **28**, 261–268 (2009).

[38]J. A. Hanley and B. J. McNeil, "A method of comparing the areas under receiver operating characteristic curves derived from the same cases," Radiology **148**, 839–843 (1983).

[39]I. Guyon, J. Weston, S. Barnhill, and V. Vapnik, "Gene selection for cancer classification using support vector machines," Mach. Learn. **46**, 389–422 (2002).

[40]H. Chai and C. Domeniconi, "An evaluation of gene selection methods for multi-class microarray data classification," in Proceedings of the Second European Workshop on Data Mining and Text Mining in Bioinfomatics, 2004, pp. 3–10.

[41]A. Rakotomamonjy, "A variable selection using SVM-based criteria," J. Mach. Learn. Res. **3**, 1357–1370 (2003).

[42]V. N. Vapnik, *Statistical Learning Theory* (Wiley, New York, 1998).

[43]K. Pelckmans, J. A. K. Suykens, T. Van Gestel, J. De Brabanter, L. Lukas, B. Hamers, B. De Moor, and J. Vandewalle, "LS-SVMlab: A Matlab/C toolbox for least squares support vector machines," available at www.esat.kuleuven.ac.be/sista/lssvmlab.

[44]J. A. K. Suykens, T. Van Gestel, J. De Brabanter, B. De Moor, and J. Vandewalle, *Least Squares Vector Machines* (World Scientific, Singapore, 2002).

[45]J. A. K. Suykens and J. Vandewalle, "Least squares support vector machine classifiers," Neural Process. Lett. **9**, 293–300 (1999).

[46]B. D. Ripley, *Pattern Recognition and Neural Networks* (Cambridge University Press, Cambridge, 1996).

[47]J. Eng, "ROC analysis: Web-based calculator for ROC curves," available at www.rad.jhmi.edu/roc.

[48]K. Kinkel, T. H. Helbich, L. J. Esserman, J. Barclay, E. H. Schwerin, E. A. Sickles, and N. M. Hylton, "Dynamic high-spatial-resolution MR imaging of suspicious breast lesions: Diagnostic criteria and interobserver variability," AJR, Am. J. Roentgenol. **175**, 35–43 (2000).

[49]B. K. Szabo, P. Aspelin, M. K. Wiberg, and B. Bone, "Dynamic MR imaging of the breast. Analysis of kinetic and morphologic diagnostic criteria," Acta Radiol. **44**, 379–386 (2003).

[50]D. Rueckert, L. I. Sonoda, C. Hayes, D. L. G. Hill, M. O. Leach, and D. J. Hawkes, "Nonrigid registration using free-form deformations: Application to breast MR images," IEEE Trans. Med. Imaging **18**, 712–721 (1999).

[51]T. Rohlfing, C. R. Maurer, Jr., D. A. Bluemke, and M. A. Jacobs, "Volume-preserving nonrigid registration of MR breast images using free-form deformation with an incompressibility constraint," IEEE Trans. Med. Imaging **22**, 730–741 (2003).

[52]C. Tanner, M. Khazen, P. Kessar, M. O. Leach, and D. J. Hawkes, "Does registration improve the performance of a computer aided diagnosis system for dynamic contrast-enhanced MR mammography?," in *Proceedings of the Third IEEE International Symposium on Biomedical Imaging: From to Nano to Macro*, 2006 (IEEE, New York, 2006), pp. 466–469.